Journal of Materials Research and Technology 38 (2025) 1185–1197

Contents lists available at ScienceDirect

Journal of Materials Research and Technology

journal homepage: www.elsevier.com/locate/jmrt

Understanding the development of mechanically and thermally induced white layers in AISI 52100 steel during hard turning: Process-microstructure-property relationship

Sahith Kokkirala [a,*], Uta Klement [a], Jonas Holmberg [b], Hirotsugu Iwasaki [c], Juan Manuel Bello Bermejo [d], Stefan Kimming [e], Seyed B. Hosseini [b,e]

[a] Industrial and Materials Science, Chalmers University of Technology, SE-412 96, Gothenburg, Sweden
[b] RISE AB, Department of Manufacturing Processes, BOX 104, Mölndal, SE-431 22, Sweden
[c] SUMITOMO ELECTRIC Hartmetall GmbH, Willich, D-47877, Germany
[d] Division of Production and Materials Engineering, Lund University, SE-221 00, Lund, Sweden
[e] AB SKF, SE-41550, Gothenburg, Sweden

ARTICLE INFO

Handling Editor: L Murr

Keywords:
Hard turning
Surface integrity
White layer
Nanocrystalline grains
Dynamic recovery
Dynamic recrystallization

ABSTRACT

Hard turning offers a cost-effective alternative to traditional grinding, yet the tool wear progression limits the broader industrial adoption. During hard turning, the surface microstructure of AISI 52100 steel transforms into a nanocrystalline structure known as white layer, accompanied by significant surface residual stresses. With optimal cutting conditions, surfaces develop nanocrystalline microstructures with high compressive stresses, known as mechanically induced white layers (M-WLs). In contrast, improper cutting conditions generate thermally induced white layers (T-WLs), associated with tensile stresses. This study investigates the effect of feed rate, cutting speed, and tool wear on the different white layers formed and their influence on the surface integrity. Microstructural analysis reveals that the M-WL formed by dynamic recovery mechanism exhibited fragmented nanocrystalline grains with ~26 % higher hardness than the bulk material. The presence of elongated lamellar grains with ~7 % higher hardness in the material drag zone beneath the M-WL suggests the occurrence of a grain subdivision process that initiates M-WL formation. This grain subdivision mechanism generated lamellar grains composed of geometrically necessary boundaries (GNBs) and incidental dislocation boundaries (IDBs), reflecting progressive strain accommodation during severe plastic deformation. In contrast, T-WL is generated by continuous dynamic recrystallization mechanism and features nanograins with ~27 % higher hardness and an underlying over-tempered dark layer with ~16 % lower hardness than the bulk material. The M-WL exhibits surface roughness of ~5 times lower and better surface compressive stress than the T-WL. This research demonstrates a promising hard turning strategy for producing advantageous M-WL with nanocrystalline grains and improved surface integrity.

List of abbreviations

PCBN	Polycrystalline cubic boron nitride
HRC	Rockwell hardness C-scale
RCF	Rolling contact fatigue
T-WL	Thermally induced white layer
M-WL	Mechanically induced white layer
TEM	Transmission electron microscopy
OM	Optical microscopy
SEM	Scanning electron microscopy
SE	Secondary electrons
V_c	Cutting speed
f	Feed rate
VB	Flank wear
a_p	Depth of cut
P	Coolant pressure
γ	Chamfer angle
XRD	X-ray diffraction
PSD	Position sensitive detectors

(continued on next column)

(continued)

(continued on next page)

* Corresponding author.
E-mail address: sahithk@chalmers.se (S. Kokkirala).

https://doi.org/10.1016/j.jmrt.2025.07.293
Received 27 May 2025; Received in revised form 31 July 2025; Accepted 31 July 2025

(*continued*)

FEG-SEM	Field emission gun - scanning electron microscopy
aSTEM	Annular scanning transmission electron microscopy
STEM-in-SEM	Scanning transmission electron microscopy in SEM
FIB	Focused ion beam
BF	Bright field
UCT	Uncut chip thickness
R_a	Average roughness
GNBs	Geometrically necessary boundaries
IDBs	Incidental dislocation boundaries
SFE	Stacking fault energy
BCC	Body centered cubic
CDRX	Continuous dynamic recrystallization
UFG	Ultra fine grains
A_{c1}	Lower critical austenitization temperature

1. Introduction

Machining processes, e.g. grinding and hard turning, generate the required surface topography, microstructural features, residual stresses, and dimensions that enable components to execute the required functions [1]. In the manufacturing industry, the grinding process is widely used to achieve high precision and good surface integrity. However, the energy input in the form of grinding forces during machining is considerably high [2]. With the development of machining technology and the advancement of new cutting tool materials, high precision and improved surface integrity can be achieved through hard turning processes with polycrystalline cubic boron nitride (PCBN) inserts [3]. The hard turning process is performed on materials with a hardness greater than 45 HRC. The advantages of hard turning compared to grinding includes lower energy consumption, higher metal removal rates, and complex machining in one setup, which reduces the cost per part [2]. However, the wider implementation of hard turning is still limited by the progression of tool flank wear, which deteriorates the surface integrity and additionally leads to increased production costs due to frequent cutting tool changes and higher scrap rate, affecting the machining efficiency [4,5].

The primary concern associated with the progression of tool flank wear is the occurrence of microstructural alterations on the machined surface. Depending on the process parameters, the interaction between worn cutting tool and workpiece material induces gradients of thermo-mechanical loads on the machined surface, resulting in the formation of a white layer [6]. Many researchers investigated the formation of white layer by various processing methods [7,8], and according to Griffiths [9], white layer formation may occur through three primary mechanisms: (a) severe plastic deformation leading to grain refinement (mechanical mechanism), (b) rapid heating and quenching resulting in phase transformation (thermal mechanism), (c) surface modification due to environmental interactions (chemical mechanism). When hard turning AISI 52100 tempered martensitic steel, the mechanical and thermal effects are primarily occurring in the formation of white layer which are induced by the combined effect of feed rate, cutting speed and tool wear [10]. Due to its superior wear resistance and high load-bearing capacity, the AISI 52100 steel is a preferred choice in bearing industries, particularly for applications involving high-stress rolling contact fatigue (RCF) conditions [11].

By adjusting the key hard turning process parameters such as cutting speed, feed rate, coolant pressure, tool chamfer angle, nose radius, and controlled tool flank wear, researchers have created white layers with different formational mechanisms [12,13]. For instance, Hosseini et al. [14] conducted a comprehensive investigation into white layer formation, demonstrating that both process parameters and tool flank wear significantly influence its microstructure development. Their results showed that thermally induced white layer (T-WL) form when the surface temperature exceeds the phase transformation threshold, while mechanically induced white layer (M-WL) occur due to severe plastic deformation at temperatures well below the phase transformation.

In T-WL, hard turning results in a further change in the material in addition to the formation of the white layer, known as the 'dark layer', which is located between the T-WL and the bulk material [15]. Both the white and dark layers exhibit different microstructural and mechanical properties compared to the bulk material. According to Guo et al. [15], the microstructure in the T-WL consists of untempered martensite, which is formed during the reverse martensitic transformation with increased retained austenite content and has a higher hardness than the bulk material. In contrast, the dark layer comprises of over-tempered martensite and is softer than the bulk material [10]. Many researchers concluded that the formation of T-WLs was due to dynamic recrystallization because of large strains, which occurred with additional driving forces from cutting temperature and phase transformation [14,16]. The combination of elevated cutting speed and progressive tool flank wear facilitated the development of a T-WL. In contrast, Hosseini et al. [14] investigated the formation mechanism of white layer at a low cutting speed of 30 m/min and reported that no dark layer formed underneath the white layer. They designated the white layer as M-WL, with a hardness approximately ~26 % higher than that of bulk. The mechanisms involved in the formation of M-WL were based on severe plastic deformation and dynamic recovery, which led to grain refinement [12,14]. Several transmission electron microscope (TEM) studies showed that the white layer consists of nanocrystalline grains with a grain size of <100 nm [13,14]. The increase in hardness of the nanostructured white layer is largely determined by the Hall-Petch effect and dislocation strengthening [17].

Cutting speed and tool wear play a major role in determining the formation of either mechanically induced or thermally induced white layer [10]. As previously reported by Chou et al. [6], the thickness of the white layer increases with the cutting speed up to a certain point and the rate of increase decreases accordingly. Also, the thickness of the white layer increases with tool wear due to its large contact area caused by thermo-plastic deformation [3]. The influence of feed rate in combination with the cutting speed and tool wear cannot be ignored as the surface roughness is largely influenced by the combined effect. As a general rule, with an increasing feed rate, the surface roughness increases [18]. Furthermore, the residual stress profiles can be used to assess the extent to which the white layers were predominantly influenced, either by thermal or mechanical energy input [19]. For example, Zhang et al. [20] found that during machining at low cutting speeds, the compressive residual stresses generated in the white layer are mainly due to the influence of plastic deformation. In contrast, during machining at higher cutting speeds, the tensile residual stresses generated in the white layer are due to the temperature influence on the machined surface. The T-WL layer exhibited increased surface hardness but exhibited lower subsurface hardness compared to the bulk material, along with tensile residual stresses that can lead to premature failure [21]. In contrast, the M-WL layer, formed through a dynamic recovery mechanism, offers more favorable properties including compressive residual stresses, increased hardness, and the absence of a softened heat-affected zone beneath the surface. These characteristics make M-WL a promising process-induced nanocrystalline surface for bearing applications. Recent work by Kokkirala et al. [18] has demonstrated that it is possible to control the formation of M-WL through precise optimization of the hard turning process and considering the cutting tool geometry, an outcome that has previously been exclusively obtained with worn cutting tools. Despite the promising characteristics of M-WL, comprehensive studies investigating the influence of hard turning process parameters on achieving low surface roughness while promoting M-WL generation are still lacking.

Therefore, a systematic study on the formation of mechanically induced white layer (M-WL) in AISI 52100 tempered martensitic steel is essential, particularly focusing on achieving reduced surface roughness and favorable compressive residual stresses under controlled hard turning conditions. Despite prior efforts, the fundamental mechanisms

governing the microstructural transformation from tempered martensite to a nanocrystalline structure in M-WL remain inadequately understood. Addressing these gaps, the present work explores both M-WL and T-WL, aiming to establish a direct correlation between processing conditions, microstructural development, and properties. The outcomes of this research are expected to contribute to the development of a novel hard turning strategy for tailoring nanocrystalline M-WL as process-induced functional surface, thereby enhancing the performance of AISI 52100 bearing steel.

2. Material and methods

2.1. Workpiece material

AISI 52100 steel with the nominal chemical composition listed in Table 1 was used in this study. The initial spheroidize-annealed cylindrical rings of 180 mm in diameter and 60 mm in height were through-hardened as follows: pre-heated at 400 °C for 120 min, followed by austenitization at ~840 °C using a controlled heating rate of ~10 °C/min. Subsequently, the samples were oil-quenched and tempered at ~240 °C to reduce retained austenite content. The final microstructure obtained after the heat treatment was a tempered martensitic matrix with μm-sized nearly spherical $(Fe, Cr)_3C$ cementite precipitates, nano-sized tempered cementite and $\leq$ 2 % retained austenite content. The hardness of the obtained microstructure was around 58–60 HRC.

2.2. Hard turning

The MONFORTS RNC500 SingleTurn machine was used for longitudinal hard turning tests in wet conditions. TiAlBN coated PCBN cutting tool inserts BNC 2125 (DNGA 1506 S01015/S01035) with a 2 mm nose radius were utilized consistently in all test scenarios. Since the hard turning is a thermo-mechanical process, the effect of individual thermal and mechanical effects cannot be completely isolated. Therefore, to understand the effect of cutting parameters on the white layer formation and the corresponding surface integrity, the cutting speed (V_c), feed rate (f), and tool flank wear (VB) were varied as shown in Table 2. The depth of cut (a_p) of 0.2 mm, the coolant pressure (P) of 150 bar, and the tool chamfer angle (γ) of 35^0 were kept constant. In total 4 tests were conducted to emphasize the predominant mechanism, whether it is thermally induced or mechanically induced. These parameters were selected based on previous experiments [18,22]. The tool flank wear (VB) = 0 indicates the tool is new. In contrast, a tool flank wear (VB) of 0.2 mm means that the tool was pre-worn to ~0.2 mm before the cutting experiment. During pre-wear treatment, a new tool was employed to machine the workpiece using an identical feed rate (f), with a cutting speed (V_c) of 110 m/min until the tool flank wear (VB) of ~ 0.2 mm was reached. Fig. 1a and b shows the sample representation with tool feed rate and workpiece cutting direction during the hard turning process.

2.3. Surface integrity

X-ray diffraction (XRD) technique was used to perform residual stress measurements using a XStress 3000 G2R diffractometer from Stresstech OY. Cr Kα X-rays (λ = 0.2291 nm) with a 2 mm collimator were used to measure the interplanar spacing of the crystal lattice with the tilt angles ranging from -45^0 to $+45^0$. Two position-sensitive detectors (PSD) were placed on the arc-shaped detectors located at 156.4^0 diffraction angle to measure the (211) lattice plane spacings with the modified $\sin^2\psi$ method. XRD was operated at a voltage of 30 kV and a current of 9 mA.

Table 1
AISI 52100 chemical composition (wt. %).

Element	C	Mn	Cr	Si	S	P	Fe
wt.%	0.95	0.32	1.42	0.26	0.001	0.009	Bal.

Table 2
Hard turning parameters used in this study.

Parameters	Cutting speed (V_c)	Feed rate (f)	Tool wear (VB)
P1	60 m/min	0,05 mm/rev	0 mm
P2	110 m/min	0,2 mm/rev	0 mm
P3	60 m/min	0,05 mm/rev	~0,2 mm
P4	110 m/min	0,2 mm/rev	~0,2 mm

Residual stresses were calculated based on elastic strain theory by applying Hooke's law using the tabulated Young's modulus parameter of 210 GPa and 0.3 Poisson's ratio as described by Noyan and Cohen [23]. The residual stresses were evaluated along the feed and cutting direction on the machined rings as shown in Fig. 1a. The depth profile was measured from the surface to 100 μm (0, 5, 10, 20, 50, 100 μm) beneath the machined surface. To perform these measurements, layer removal was performed applying an electropolishing technique using a salt electrolyte and a dial gauge to measure the depth removed.

Surface roughness analysis was performed to determine the R_a parameter on machined surface generated under different cutting conditions. The measurements were performed by Sensofar S Neox 3D optical profilometer equipment using the coherence scanning interferometry technique with 10× magnification. Three measurements were performed on the hard-turned rings over a 7.4 × 1.3 mm area with a uniform lateral resolution of 1.29 μm and the results were averaged. The data obtained was analyzed using 2nd-order polynomial fit for form removal. The data was filtered using a spatial medium noise reduction filter with a window size of 5 x 5 points to reduce the short wavelength noise. The data collected was then analyzed using Digital Surf's MountainsMap software.

2.4. Microstructural characterization

For the microstructural characterization, the samples were cut using a Struers cutting machine and hot-mounted in a 40 mm diameter conducting polyfast bakelite using CitoPress 20. The samples were wet ground on 220-grid SiC paper followed by polishing with 9 μm, 3 μm and 1 μm diamond paste suspension on the respective polishing cloths for 6 min, 6 min, and 3 min, respectively, using Struers Tegrapol machine to have a mirror-finished sample. To reveal the white and dark layers on the machined surface, a 2 % Nital etchant was used for 7–10 s. The mounted polished and etched cross-section sample was investigated using a Zeiss Axioscope 7 optical microscope (OM). The Nital etchant resulted in contrasting images that highlighted the white and dark layers in the cross section.

Since the detailed microstructure of the white layer cannot be resolved by OM, a Zeiss Gemini 450 scanning electron microscope with field emission gun (FEG-SEM) was used to analyze the microstructural features. Imaging was done with secondary electrons (SE) at 3 kV, 500 pA, and a working distance of 5–6 mm. Samples etched with 2 % Nital solution were used for SE imaging.

To investigate the morphology of the white layers by use of annular scanning transmission electron microscopy (aSTEM) detector in the Gemini 450 FEG-SEM (STEM-in-SEM), samples were prepared using a site-specific focused ion beam (FIB) lift-out technique in the FEI Versa 3D equipment. To protect the machined surface, a platinum layer was deposited on the surface and the FIB milling was performed at 30 kV with decreasing currents ranging from 15 nA to 50 pA to reduce the beam damage on the sample. Afterwards, the final polishing steps were performed at 5 kV and 2 kV with 48 pA and 27 pA, respectively. The final thickness of the lamella was around 80–100 nm. aSTEM bright field (BF) imaging was performed in the Gemini 450 FEGSEM at 30 kV accelerating voltage, 500 pA current, and with a working distance of 3.8 mm–4 mm.

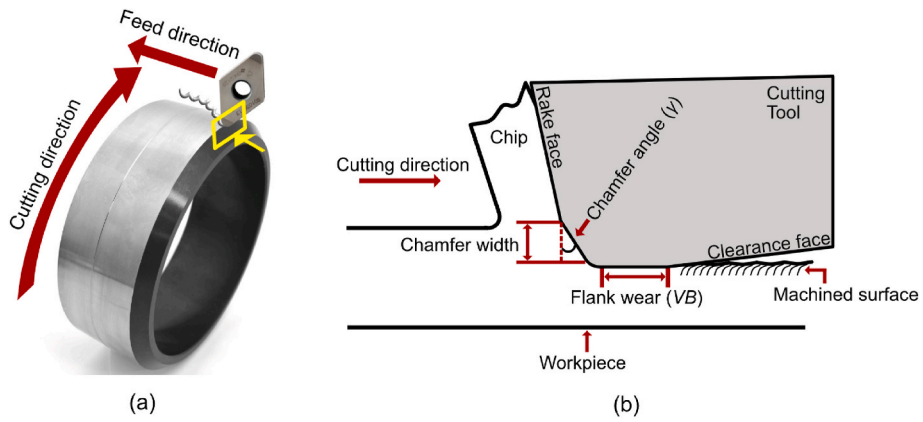

Fig. 1. (a) Sample representation with feed and cutting direction during the hard turning process. (b) Schematic of tool geometry in contact with the workpiece from the point of view of the yellow rectangular box.

2.5. Nanoindentation

Nanoindentation measurements were conducted on the machined white layer surface using a NanoTest Vantage nanoindentor from Micro Materials Ltd., which was equipped with a diamond Berkovich tip. Indentations were performed using load-controlled condition with a maximum load of 4 mN. The measurements were performed with a loading time of 10 s, dwell time of 10 s at max load, and 10 s of unloading time. Thermal drift correction was enabled with 30 s data collection. Data analysis was conducted using the Micro Materials software for calculating the hardness using load-displacement curves by using the Oliver-Pharr method [24]. To accurately measure the hardness values of the white layer without the presence of μm-sized nearly spherical $(Fe, Cr)_3C$ cementite precipitates, after the nanoindentation tests, the indentations were examined by SEM to confirm the positions.

3. Results

3.1. Residual stresses

Fig. 2a and b shows the residual stress profiles for P1, P3 and P2, P4 from the machined surface down to a depth of 100 μm. Each graph consists of 4 profiles, representing feed and cutting direction measurements for each parameter. For sample P1 (Fig. 2a) along the feed direction, the residual stress profile showed a "grinding" profile rather than the typical "hook-shaped" profile normally seen on hard-turned surfaces, when machined at a feed rate of 0.05 mm/rev and a cutting speed of 60 m/min using a new cutting tool surface [25]. In the hook-shaped stress profiles, the maximum compressive residual stresses are present below the machined surfaces, while the residual stress profiles that often occur after grinding have their maximum compressive stresses on the surface. The corresponding machined workpiece with grinding shape profils exhibited compressive stress of −771 MPa on their surface, with the compressive stresses below the surface gradually decreasing with increasing depth. The affected region extended to a depth of 20 μm from the surface. But in the cutting direction, "hook--shape" behavior is observed for sample P1. The magnitude of surface compressive stresses measured along the cutting direction is with a value of −81.5 MPa notably lower compared to the feed direction. When transitioning from a fresh insert to a worn insert with a flank wear of 0.2 mm in Fig. 2a, the magnitude of subsurface residual stresses changed. This change results in maximum compressive stresses occurring at depths between 5 and 50 μm from the surface, with the affected region extending beyond 100 μm. As depicted in Fig. 2a for sample P3, the surface compressive stresses along the feed direction are significantly higher when machined with a low feed rate of 0.05 mm/rev and cutting speed of 60 m/min, reaching −1351 MPa. However, with similar cutting parameters, the measured surface compressive stresses along the cutting

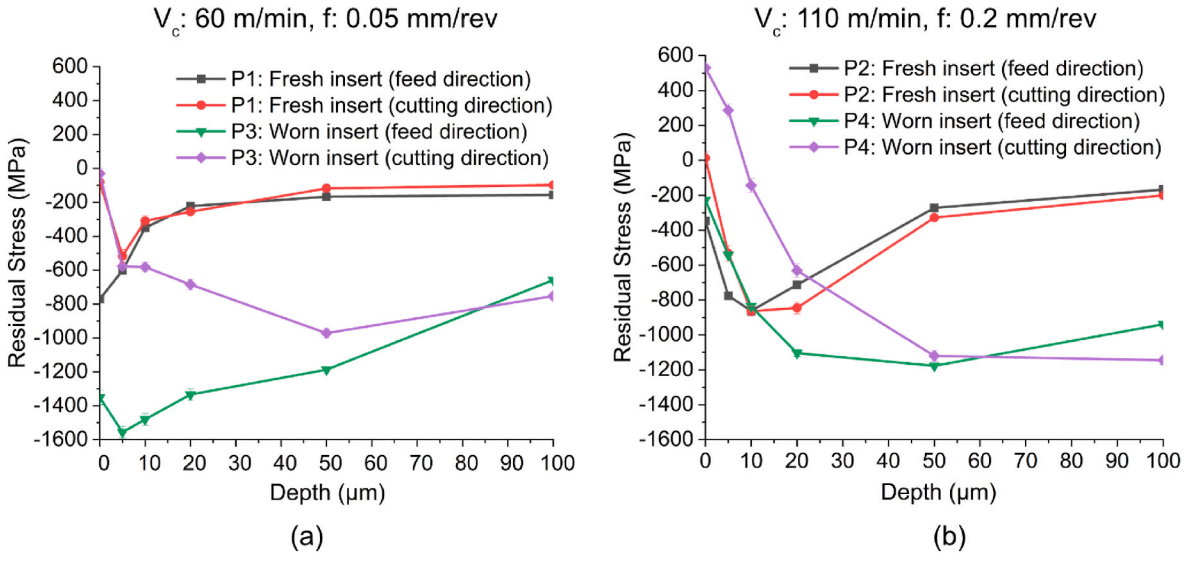

Fig. 2. Residual stress profiles for the cutting parameters (a) Vc: 60 m/min, f: 0.05 mm/rev, (b) Vc: 110 m/min, f: 0.2 mm/rev.

direction are −30 MPa.

When the cutting speed is increased to 110 m/min and feed rate increased to 0.2 mm/rev (sample P2), lower surface compressive stresses were observed compared to sample P1 in Fig. 2b, which are related to the increase in the cutting temperatures. However, with an increased feed rate and cutting speed, the subsurface regions in sample P2 showed higher compressive stresses compared to sample P1. In this case, the highest compressive stresses are observed at a depth of 10 μm and the affected region extends to a depth of 50 μm. For sample P4, machined with worn insert along the feed direction, the surface compressive stress decreased to −227 MPa along the feed direction compared to sample P3 due to the higher temperatures in the tool/workpiece contact zone. Specifically, along the cutting direction, the sample P4 exhibited surface tensile stress of 530.5 MPa.

3.2. Surface roughness

The average surface roughness (R_a), for different machining conditions is shown in Fig. 3a and b. The influence of feed rate can be clearly observed for the different cutting conditions. The surface roughness was measured to be 0.11 μm for the P1 fresh insert and 0.19 μm for the P3 worn insert when using a low feed rate of 0.05 mm/rev and a low cutting speed of 60 m/min. This can be compared to a value of ~0.2 μm obtained from the grinding process [26]. As the feed rate and cutting speed increases, the surface roughness increases significantly to 0.59 μm for sample P2 and 1.19 μm for sample P4.

The surface roughness degraded when machined with a worn insert having 0.2 mm flank wear, as observed in Fig. 3a. This deterioration is attributed to the irregularities generated on the tool flank face with increased tool wear. However, the measured roughness values for the worn insert are lower at a low feed rate of 0.05 mm/rev than those obtained from samples machined with fresh inserts at a higher feed rate of 0.2 mm/rev, which highlights the significant influence of feed rate on surface roughness.

3.3. Mechanically and thermally induced white layers

The initial microstructure of quenched and tempered AISI 52100 steel before hard turning is shown in Fig. 4a and b, showcasing an optical microscopy (OM) image and a scanning electron microscopy (SEM) image after etching with 2 % Nital. The secondary electron (SE) image in Fig. 4b shows the microstructural constituents of the tempered martensite. The yellow arrows indicate μm-sized nearly spherical (Fe, $Cr)_3C$ cementite precipitates and the red arrows indicate nano-sized tempered cementite within the martensite structure.

Fig. 5 shows cross-sectional OM images of samples produced during hard turning, where either mechanically or thermally induced white layers were formed along the feed direction. White layers with different thicknesses are visible on all four machined surfaces. The samples in Fig. 5a and b, which are machined with a feed rate (f) of 0.05 mm/rev and cutting speed (V_c) of 60 m/min, show no dark layer underneath the white layer. As described by Fang-yuan et al. [3], the thickness of the white layer increased when machined with a worn insert with a flank wear of VB: ~0.2 mm. In contrast, in the samples machined with a feed rate of 0.2 mm/rev and cutting speed of 110 m/min shown in Fig. 5c and d, both white and dark layers are clearly visible. The dark layer observed in Fig. 5c is very thin and discontinuous and has formed at the end of the feed groove. The dark layer in Fig. 5d is thicker compared to Fig. 5c because the increased flank wear leads to a larger thermal effect under the specific cutting condition.

The machined surfaces that form a white layer without an adjacent dark layer are known as mechanically induced white layers (M-WLs). These M-WL surfaces can be categorized based on the condition of the cutting tool, when machined with a fresh insert, they are referred to as M-WL (Fresh), and when machined with a worn insert, they are called M-WL (Worn). In contrast, thermally induced white layers (T-WLs) are characterized by the presence of both white and dark layers. Like M-WL, T-WL surfaces are classified as T-WL (Fresh) when machined with a fresh insert, and T-WL (Worn) when machined with a worn insert. Due to the etch-resistant fine-grained structure of the white layer, OM images do not reveal their microstructural details.

Fig. 6a–d shows exemplary SE−SEM images of the samples with M-WL (Fresh), M-WL (Worn), T-WL (Fresh), and T-WL (Worn). The average thickness of the white layer for M-WL and T-WL when using a fresh insert is between 0.7 and 1.5 μm and varies along the feed direction. The dark layer thickness for T-WL (fresh) is approximately 0.5 μm. When using worn inserts, the average white layer thickness increases to 2–3 μm in both M-WL and T-WL and the dark layer thickness for T-WL (Worn) ranges between 3 and 4 μm.

In Fig. 7a and b, the morphology of the M-WL and T-WL obtained using a worn insert is shown. The M-WL (Worn) shown in Fig. 7a exhibits a fine fragmented elongated grain structure, contrasting with the bulk structure. Yellow circles mark the fragmented nearly spherical.

$(Fe, Cr)_3C$ cementite particles in this region. Beneath the white layer, a plastically deformed, elongated grain structure is visible in the material drag region, which has a thickness of 1 μm. Here, the grain structure is elongated along the feed direction but not fragmented. Fig. 7b shows the T-WL (Worn), which is characterized by a fine structured morphology in the region of the white layer. In contrast to the observation in M-WL, no carbide fragmentation in the T-WL is observed. Below the white layer, an over-tempered dark layer region can be found. Comparing with the bulk microstructure shown in Fig. 7c, the M-WL in Fig. 7a and the T-WL in Fig. 7b consist of refined grains at the machined surface and show a different morphology.

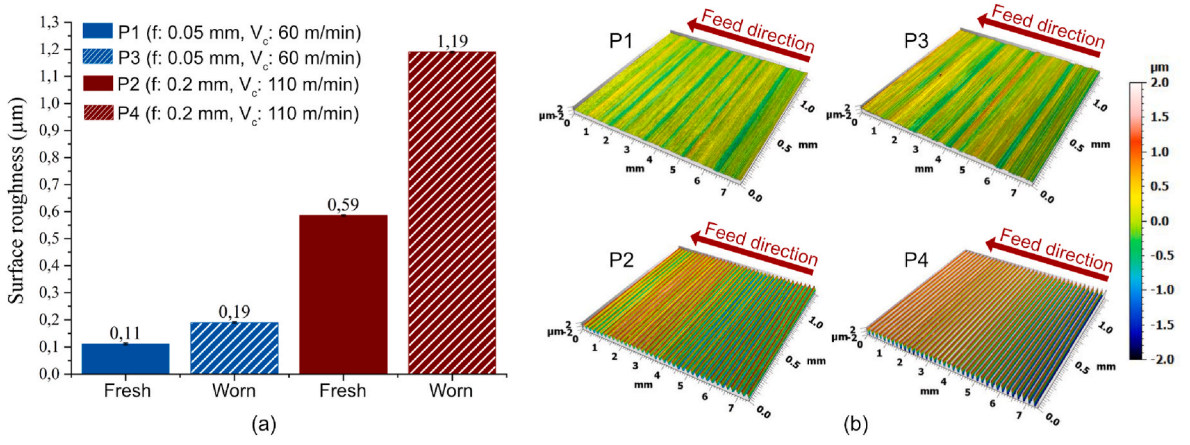

Fig. 3. (a) Surface roughness values for hard turning cutting parameters, (b) Surface topography graphs of sample machined with P1, P2, P3, and P4 parameters.

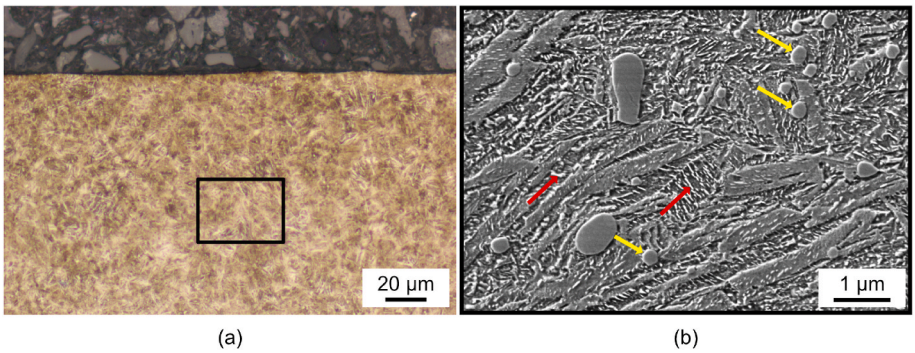

Fig. 4. Images of the tempered martensite bulk microstructure. (a) OM image with 500× magnification, and (b) SE−SEM image with 35kx magnification. The yellow arrows indicate μm-sized nearly spherical $(Fe, Cr)_3C$ cementite precipitates and the red arrows indicate nano-sized tempered cementite.

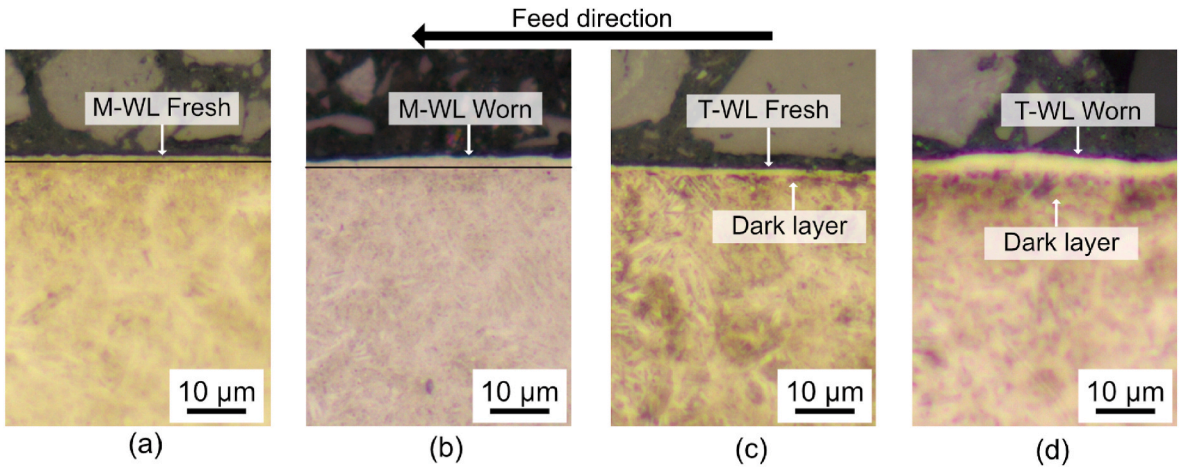

Fig. 5. Optical microscopy images of the mechanically and thermally influenced machined samples along the feed direction (500× magnification). (a) Fresh insert, f: 0.05 mm/rev, V_c: 60 m/min (M-WL Fresh) (b) VB: ~0.2 mm worn insert, f: 0.05 mm/rev, V_c: 60 m/min (M-WL Worn), (c) Fresh insert, f: 0.2 mm/rev, V_c: 110 m/min (T-WL Fresh), and (d) VB: ~0.2 mm worn insert, f: 0.2 mm/rev, V_c: 110 m/min (T-WL Worn).

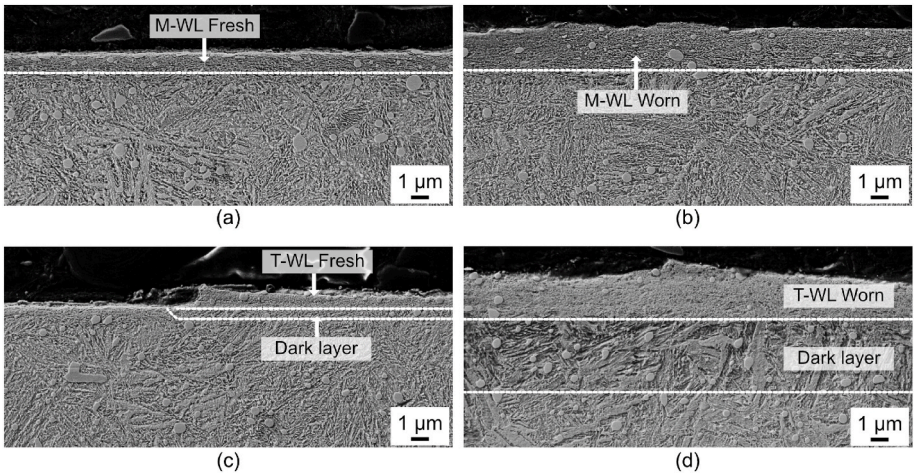

Fig. 6. SE−SEM images of samples machined along the feed direction (10kx magnification). (a) Fresh insert, f: 0.05 mm/rev, V_c: 60 m/min (M-WL Fresh) (b) VB: ~0.2 mm worn insert, f: 0.05 mm/rev, V_c: 60 m/min (M-WL Worn), (c) Fresh insert, f: 0.2 mm/rev, V_c: 110 m/min (T-WL Fresh), and (d) VB: ~0.2 mm worn insert, f: 0.2 mm/rev, V_c: 110 m/min (T-WL Worn).

To further examine the morphology of the white layers, an annular STEM detector in the SEM (STEM-in-SEM) is utilized. The white layers generated by the worn tool are analyzed, as they exhibit a thicker white layer compared to those generated by fresh inserts. In Fig. 8a, the M-WL on the machined surface generated under cutting conditions of V_c: 60 m/min and f: 0.05 mm/rev is shown together with the material drag region. The grains in the M-WL region are elongated, rectangular nanocrystalline grains aligned in feed direction, with some grains as small as ~10 nm, as shown in Fig. 8c. In contrast, the material drag region along the feed direction exhibits a bent and deformed martensite structure,

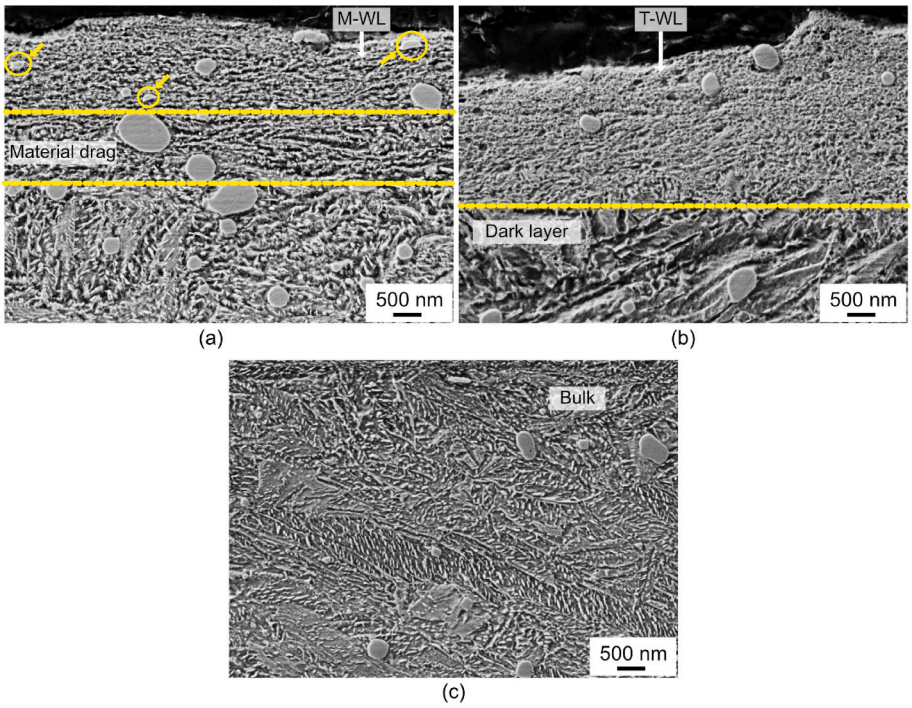

Fig. 7. High magnification SE−SEM images (35kx magnification). (a) M-WL consisting of fine fragmented elongated grain structure; yellow circles indicate fragmented spherical cementite particles accompanied by material drag underneath, (b) T-WL consisting of fine structured morphology accompanied by a dark layer underneath, and (c) Bulk tempered martensite AISI 52100 steel.

containing distinct elongated lamellar grains indicating severe plastic deformation, as shown in Fig. 8e. This is due to a decreasing gradient of plastic strain from the surface to the bulk. The higher plastic strain in the M-WL region has fragmented the grains into a nanocrystalline structure, while in the material drag region, with a lower plastic strain gradient, a deformed and elongated microstructure is found. In the material drag region as shown in Fig. 8e, the lamellar grains formed by plastic deformation are characterized by the geometrically necessary boundaries (GNBs) marked in dashed yellow, while the interconnected boundaries inside each domain of the GNBs are known as incidental dislocation boundaries (IDBs) [27]. Typical examples of IDBs are dislocation cell boundaries, as observed in Fig. 8e marked in light blue.

Fig. 8b shows the STEM-in-SEM image of the T-WL and the dark layer beneath it. In contrast to the M-WL shown in Fig. 8a, the T-WL does not exhibit any plastic deformation beneath it, indicating a different formation mechanism. As shown in Fig. 8d, the grain size of the T-WL is about 40 nm–100 nm. Few grains in the T-WL region are equiaxed and contain a high dislocation density. In addition, some nearly spherical $(Fe, Cr)_3C$ cementite precipitates are visible and appear to be unaffected, as shown in Fig. 8b. No fragmentation is observed, although the nano-sized tempered cementite precipitates might have dissolved due to the heating effect. In contrast, the dark layer beneath the T-WL shows a martensite structure without any deformation, with nano-sized tempered cementite clearly visible within the tempered martensite structure, as shown in Fig. 8f.

3.4. Nanoindentation

Samples with white layers generated by worn inserts, M-WL (Worn) and T-WL (Worn) were selected because they have thicker layers more suitable for nanoindentation. Fig. 9a and b illustrates the nano-hardness values for both M-WL and T-WL samples. The bulk nano-hardness value of the sample is determined to be 9.1 ± 0.3 GPa. In both samples, the white layer region exhibits higher hardness than the bulk material. The hardness of M-WL is 11.5 ± 0.4 GPa, which is ~26 % higher than the hardness compared to the bulk material. As seen in Fig. 9a, the material drag region underneath the M-WL has a hardness of 9.7 ± 0.3 GPa, which is ~7 % harder compared to the bulk material. Additionally, the influence of severe plastic deformation is evident around the nearly spherical $(Fe, Cr)_3C$ cementite particles, with a distinctive plastic flow of martensite structure as shown in Fig. 10b. The hardness of the T-WL is 11.6 ± 0.64 GPa, which is ~27 % harder than the bulk material. The dark layer observed underneath the T-WL has a hardness of only 7.6 ± 0.48 GPa, which is ~16 % softer than the bulk material, as shown in Fig. 9b. Similar hardness values in the white layers are reported by Akcan et al. [16] with grain size in the range of 30 nm–500 nm.

4. Discussion

In the hard turning process, the machined surface is a product of the thermo-mechanical interaction between the cutting tool insert and the workpiece material. The fundamental nature of white layer formation is determined by the cutting conditions as observed in Fig. 5. The effect of process parameters and microstructural development of M-WL and T-WL is further discussed.

4.1. Mechanically induced white layers

4.1.1. Effect of process parameters on M-WL surface integrity

The M-WL generated with both fresh and worn inserts by using a low feed rate of 0.05 mm/rev and a low cutting speed of 60 m/min, exhibits higher compressive stresses in the feed and cutting direction as illustrated in Fig. 2a. This is because higher cutting forces are required to shear the material as the thermal softening effect is lower. For the P1 sample along the feed direction, the possible reason to exhibit grinding profile is at low feed rates, the uncut chip thickness (UCT) becomes significantly smaller than the tool tip radius, causing the effective rake angle to become largely negative. This puts the material ahead of the tool's cutting edge into a highly compressive stress state. Consequently, this causes a large amount of material to be plastically deformed before a thin chip is created, resulting in an overall "grinding profile" for the hard turning process [25,28]. Furthermore, in hard turning, the thrust force

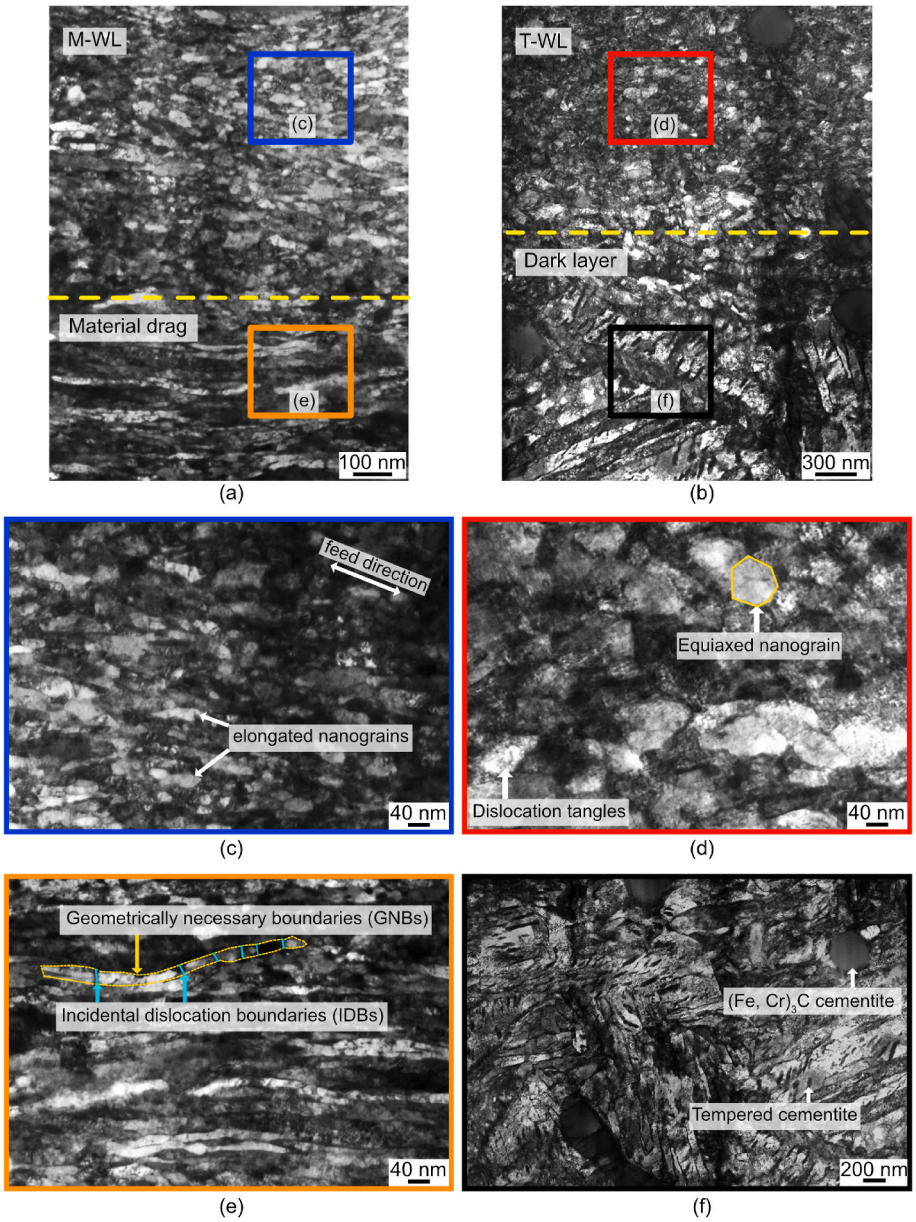

Fig. 8. STEM-in-SEM BF images of the predominantly mechanically and thermally induced machined samples along the feed direction. (a) Overview of the M-WL (Worn) with material drag beneath (70kx magnification), (b) Overview of the T-WL (Worn) with dark layer beneath (25kx magnification), (c) M-WL with nanocrystalline grains (150kx magnification), (d) T-WL with nanocrystalline grains (150kx magnification), (e) Grain subdivision mechanism with GNBs and IDBs observed within the lamellar grain in the material drag zone beneath the M-WL (150kx magnification), (f) Over tempered martensite with nearly spherical $(Fe, Cr)_3C$ cementite precipitates and nano-sized tempered cementite observed in the dark layer region beneath the T-WL (30kx magnification).

increases due to large contact area of tool wear, leading to a higher mechanical impact on the subsurface regions [5]. The thickness of the M-WL increased with the progress of the tool wear because of intensified plastic deformation and increased strain in the workpiece material caused by the larger tool flank wear (greater duration of contact between tool and workpiece). The effect of increased tool wear is also observed in the residual stresses along the feed direction, as the compressive residual stresses at the surface increased from −771 MPa for the fresh insert to.

−1351 MPa for the worn insert. In a study by Hosseini et al. [29], cutting temperatures were measured using a two-colour pyrometer method for AISI 52100 bearing steel machined using a PCBN insert. At a cutting speed of 30 m/min, the temperatures for a fresh insert were ~510 °C and for a worn insert ~540 °C, using a constant feed rate of 0.08 mm/rev. These results suggest that temperatures for M-WL generated at a feed rate of 0.05 mm/rev and cutting speed of 60 m/min remain below the critical austenitization temperature (A_{c1}), indicating the effect of severe plastic deformation. Similar observations of white layers generated below austenitization temperature were previously reported by Refs. [13,14]. Additionally, regarding the surface roughness values observed in Fig. 3a, lower feed rate resulted in a smoother surface finish for the P1 and P3 samples. This is due to the distance between the peaks and valleys in the generated feed marks are smaller as shown in Fig. 3b compared to P2 and P4 samples. This phenomenon is attributed to the formation of helicoid furrows [30], which occur due to the relative displacement between tool and workpiece surfaces. The tool flank wear condition (P3) resulted in a more pronounced increase in surface roughness (Ra) compared to P1. This deterioration is attributed to the irregularities generated on the tool flank face with increased tool wear.

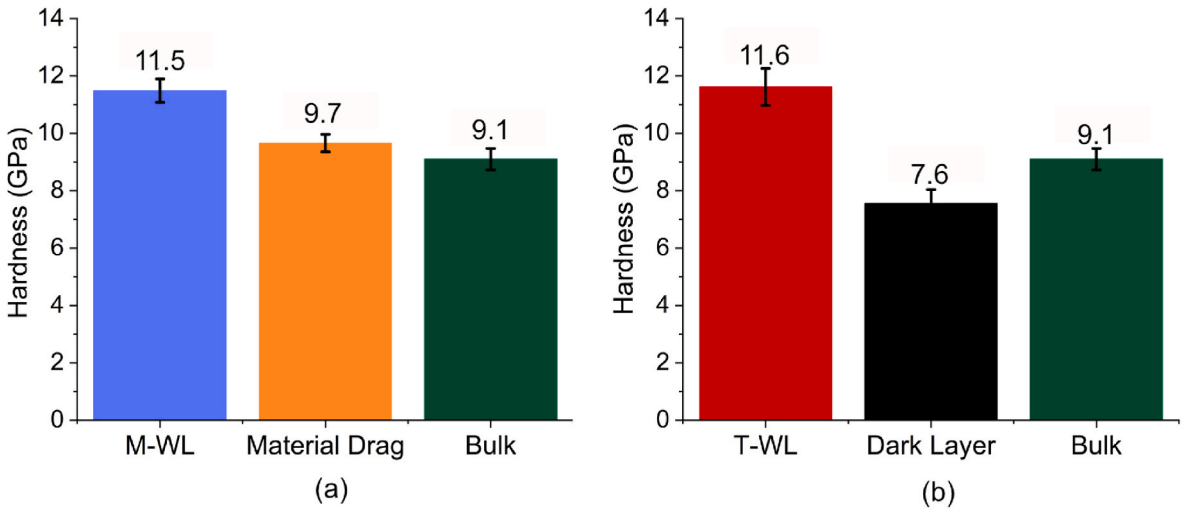

Fig. 9. Nanoindentation results of the machined samples. (a) M-WL with material drag underneath, and (b) T-WL with the dark layer underneath.

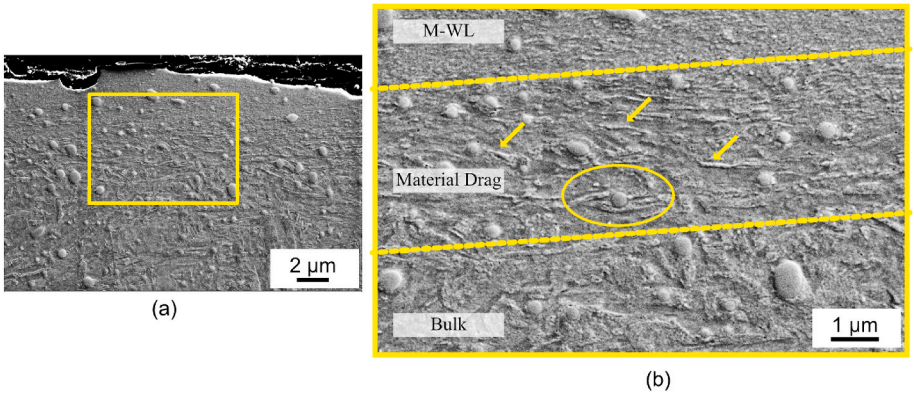

Fig. 10. (a) SE−SEM image of the M-WL produced with a worn cutting tool. (b) Material drag is clearly visible due to the elongated microstructure. Arrows indicate the elongated martensite structure, while the elongated martensite flow lines around the spherical cementite is circled.

4.1.2. Microstructural development of M-WL

During thermo-plastic deformation in the hard turning process, the free energy of the material increases due to the increased dislocation density caused by the deformation, which leads to work hardening and an influence on the flow stresses. At this stage, a significant number of dislocations begin to emerge, but the grain morphology remains unchanged due to the relatively low plastic strain. As deformation progresses, adiabatic shear initiates, causing a sharp rise in dislocation density. The material containing these defects is believed to be thermodynamically metastable [31]. Additionally, the intense plastic slip leads to the reorientation and elongation of the grain structure along the shear direction, forming lamella-shaped GNBs through the grain subdivision process. As deformation localization intensifies, dislocations begin to climb, resulting in the formation of dislocation cells with IDBs, as shown in Fig. 8e [27]. Tsuji et al. [32] observed a similar elongated deformed microstructure produced by the accumulative roll bonding process with a strain of 5.6 at 500 °C. Hughes et al. [27] studied the formation of deformation microstructures and ultrafine grain structures and referred to the elongated grain deformation caused by severe plastic deformation as the grain subdivision process. When the material is strained, plastic deformation causes the original grains to subdivide into GNBs and IDBs, a process evident in the material drag region of the M-WL as observed in Fig. 8e. The observed ~7 % of increased hardness in the material drag region is due to the higher dislocation density caused by intense mechanical strains, leading to the formation of lamellar grains. In this context, the elongated deformed lamellar grains in the material drag region signify an initiation stage in the formation of M-WL, a phenomenon not previously documented in AISI 52100 tempered martensitic steel subjected to hard turning. Further, the dynamic recovery process begins with the annihilation and rearrangement of dislocations. In this scenario, the rate of defect generation, marked by an increase in dislocations, surpasses the rate of dislocation annihilation. As a result, only partial elimination of dislocations takes place under these conditions [31]. Supported by the local temperature increase caused by localized plastic deformation, dislocation entanglements form, creating regions with higher dislocation densities and leading to the development of subgrain boundaries. These subgrain cell walls eventually segment, resulting in the refinement of elongated grains into nanocrystalline grains (M-WL), as observed in Fig. 8c [33,34]. The ~26 % increased hardness of the nanocrystalline grains in the M-WL can be attributed to grain boundary strengthening via the Hall-Petch effect due to their small grain size. Dislocation climb plays a vital role in dynamic recovery, and in metals with high stacking fault energy (SFE) such as BCC steels, this climb occurs rapidly [13]. The M-WL generated under these high strain rate cutting conditions is primarily a result of the dynamic recovery mechanism associated with severe plastic deformation. Fig. 11a–d schematically illustrates and summarizes the above-mentioned M-WL and material drag development mechanisms in AISI 52100 tempered martensitic steel.

In addition, some nearly spherical $(Fe, Cr)_3C$ cementite precipitates in the M-WL region have been fragmented, as shown in Fig. 7a, and nano-sized tempered cementite is absent in this region, as seen in Fig. 8c

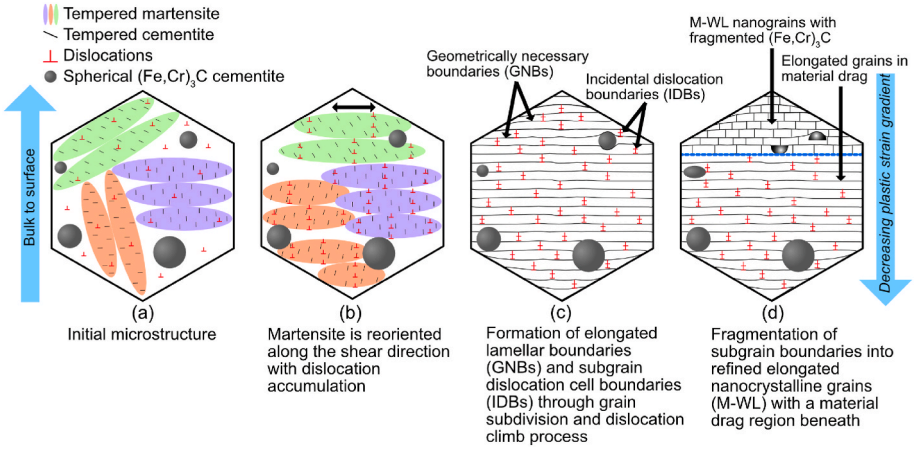

Fig. 11. Schematic illustration of M-WL microstructural development driven by dynamic recovery associated with severe plastic deformation during hard turning.

compared to Fig. 8f. A similar observation was reported by Hosseini et al. [14] and Zhang et al. [35], who noted that with increasing strain rates and strain, the local stress concentration at the matrix/tempered cementite interface may exceed the shear strength of the cementite particles, leading to their deformation or fragmentation. As seen in Fig. 4b, the nano-sized, rod-like cementite initially forms during the second stage of tempering at ~240 °C [36]. This formation occurs through the decomposition of retained austenite into ferrite and cementite. It is possible that during the formation of M-WL, this tempered cementite does not dissolve but instead deforms along the GNBs [37]. Nevertheless, conclusive evidence of tempered cementite's presence within the material drag region and the M-WL requires further investigation. Additionally, Kagawa et al. [38] reported on the hot hardness of (Fe, Cr)$_3$C cementite precipitates, observing that, depending on the chromium content, the hardness decreased by 27.5 % when the temperature increased from 200 °C to 550 °C. From the surface to the bulk, the microstructure varies as a result of varying strain, strain rates and temperature induced during the hard turning process. By hard turning with a feed rate of 0.05 mm/rev and a cutting speed of 60 m/min, a tailored microstructure featuring mechanically induced nanocrystalline grains and deformed grains beneath the surface is achieved, resulting in higher compressive stresses, lowered surface roughness, and an improved hardness gradient from surface to bulk.

4.2. Thermally induced white layers

4.2.1. Effect of process parameters on T-WL surface integrity

As shown in Fig. 5c and d, the T-WLs generated under high cutting speed conditions of 110 m/min and a high feed rate of 0.2 mm/rev is characterized by the presence of a dark layer underneath. As the feed rate increased to 0.2 mm/rev and cutting speed increased to 110 m/min for the P2 and P4 samples, lower surface compressive stresses were observed compared to P1 and P3 samples, which are associated with the rise in the cutting temperatures. The effect of feed rate on the cutting temperatures was studied by Outeiro et al. [39] and Hua et al. [40] who mentioned that there is an increase in cutting temperature with feed rate. The rise in cutting temperature results from the fact that with increasing feed rate the chip thickness increases and thus ultimately the cutting forces also increase. The higher material removal rate associated with increased feed rates leads to greater heat generation and increased cutting energy, consequently resulting in lower surface compressive stresses with material softening effect [40]. However, with an increase in feed rate to 0.2 mm/rev, the subsurface regions exhibited higher compressive stresses. During hard turning, the higher feed rate increases the cutting temperature, favoring plastic deformation beneath the tool flank face and causing significant tensile plastic deformation. The tensile strain increases with the feed rate due to higher cutting forces. This means that the tensile deformation in the area below the flank face, directly behind the cutting edge, extends to greater depths. The stress state reverses when the deformation zone is unloaded, resulting in higher subsurface compressive stresses [39]. As reported by Hosseini et al. [29], the cutting temperatures were measured using a two-colour pyrometer method for AISI 52100 bearing steel machined using a PCBN insert. For the feed rate of 0.08 mm/rev and cutting speed of 110 m/min, the measured cutting temperatures were ~810 °C with a fresh insert and ~880 °C with a worn insert indicating the occurrence of phase transformation. In Fig. 6c, the dark layer created with a fresh insert appears very thin, whereas the worn insert resulted in a thicker white and dark layer as shown in Fig. 6d. This increase in thickness is due to higher temperatures generated by the worn insert, resulting in a deeper heat-affected zone due to increased frictional contact between the tool and the workpiece. According to previous research findings, the temperatures measured during the formation of T-WL exceeding the A_{c1} temperature range [29,41]. The observed residual stresses in the cutting direction indicated approximately 530 MPa of surface tensile residual stresses for the worn insert, highlighting the significant influence of thermal effects. This is due to the influence of high cutting forces compared to feed forces and the increase in surface temperatures due to the frictional heat along the cutting direction due to the larger contact zone [42]. Additionally, increasing the feed rate and cutting speed resulted in increased R_a as shown in Fig. 3a. As the feed rate increases for samples P2 and P4, the helicoid furrows become wider and deeper, resulting in an increase in surface roughness, as shown in Fig. 3b compared to P1 and P3 parameters. The average spacing between the two peaks corresponds to the feed rate as shown in Fig. 3b.

4.2.2. Microstructural development of T-WL

As shown in Fig. 7b, the T-WL generated under high cutting speed conditions of 110 m/min and a high feed rate of 0.2 mm/rev is characterized by the presence of a dark layer underneath. Also, the morphology observed for T-WL in SEM (Fig. 7b) is different from M-WL (Fig. 7a). At 110 m/min cutting speed and 0.2 mm/rev feed rate, large friction between the workpiece and the cutting tool with tool wear of 0.2 mm results in the generation of high heat and plastic deformation on the machined surface. The dynamic recovery mechanism sets in, but as the temperature exceeds the phase transformation temperature because of the higher cutting speed, the initial BCC/BCT tempered martensite microstructure changes to FCC austenite phase. Additionally, the substantial energy stored in the deformed elongated grains, resulting from the strain during the dynamic recovery process, significantly reduces the recrystallization temperature [43]. When the material is in the austenite FCC phase, the stored energy surpasses a critical threshold where the work hardening, and recovery can no longer store immobile dislocations. A more intense restoration process known as dynamic

recrystallization inevitably takes place usually in low SFE austenite phase. At 1000 °C, BCC iron exhibits a high stacking fault energy (SFE) of 0.2 J/m^2 as compared to FCC iron, which has an SFE of 0.075 J/m^2 [13]. Metals with low SFE face difficulties in dislocation climb out of their glide planes and alloys that exhibit slow dynamic recovery due to low SFE are more susceptible to undergo dynamic recrystallization [43]. The decrease in stacking fault energy (SFE) caused by the phase transformation may promote the occurrence of dynamic recrystallization [13]. Given the extremely short timescale of the cutting process, typically on the order of microseconds, the discontinuous dynamic recrystallization based on diffusion controlled grain boundary migration is unlikely to occur [44]. Instead, mechanically assisted progressive subgrains rotation mechanism associated with continuous dynamic recrystallization (CDRX) refine the austenite grains to nanometer range [34,45]. Due to the high cooling rates, the newly recrystallized austenite grains quenched to form un-tempered martensite resulting in the T-WL. As reported by Hosseini et al. [29], the cooling rates during hard turning reach as high as $>10^4$ ^{0}C/s. Although the grain size in this region is slightly larger than in the M-WL, as shown in Fig. 8d compared to Fig. 8c, the reverse martensitic transformation led to the formation of BCT untempered martensite, driven by dynamic recrystallization and grain growth mechanisms. The carbon solid solution strengthening in the nanocrystalline grains with carbon atoms arranged at grain boundaries in the T-WL, combined with the increased dislocation density as shown in Fig. 8d, probably explains the similar hardness values to the M-WL, although the M-WL has smaller nanocrystalline grains [37]. The absence of intense plastic deformation in the T-WL suggests that the phase transformation temperature was reached quickly, preventing the formation of subsurface GNBs and IDBs as seen in the material drag region beneath the M-WL (Fig. 8a). This indicates a stronger influence of thermal effects under the cutting conditions Vc: 110 m/min, f: 0.2 mm/rev, and additionally, the tool wear further accelerates the overall effect. The ~16 % decrease in hardness in the dark layer is a result of the high-temperature tempering process. Similarly, Akcan et al. [16] reported that the dark layer formed underneath the T-WL is due to the over-tempering process. The temperature distribution of the machined surface exhibits a gradient profile, as the cutting heat transferred into the subsurface decreases with increasing distance from the machined surface. When the temperature of the subsurface falls below the austenite phase transformation temperature, the formation of the white layer is inhibited, and the over-tempered dark layer is observed.

Reza et al. [46] investigated the grain refinement mechanisms in BCC ferrite steel and FCC austenite steel under highly deformed conditions at high strain rates and temperatures. They reported that the equiaxed ultrafine grains (UFG) in FCC austenite steel resulted from grain subdivision and dynamic recrystallization, while the BCC ferritic steel displayed lamellar UFG structures due to grain subdivision, which is part of the dynamic recovery mechanism. It is widely accepted that dynamic recrystallization is commonly inhibited in ferritic steels with high stacking fault energy, as enhanced dynamic recovery reduces dislocation density and the driving force for recrystallization. Furthermore, Barry and Byrne [13] concluded that T-WL has high retained austenite content due to the reverse martensitic transformation, which is attributed to the transition from dynamic recovery to dynamic recrystallization. This transition results in the formation of fine equiaxed nanocrystalline grains in T-WL as shown in Fig. 8d with no visible severe plastic deformation compared to elongated rectangular nanocrystalline grains in M-WL as shown in Fig. 8c. The T-WL generated under these high strain rate and high temperature cutting conditions is primarily a result of the dynamic recovery mechanism followed by dynamic recrystallization mechanism in association with reverse martensite transformation. Fig. 12a–d schematically illustrates and summarizes the above-mentioned T-WL and dark layer development mechanisms in AISI 52100 tempered martensitic steel.

5. Conclusions

This study investigates the microstructural development and surface integrity of both M-WL and T-WL with the aim of establishing a clear relationship between processing, microstructure, and properties with a particular focus on developing high-performance nanocrystalline M-WL as a process-induced functional surface on AISI 52100 bearing steel. The following conclusions are drawn from the study.

- Depending on the process parameters, hard turning generated two types of WLs, mechanically induced white layer (M-WL) and thermally induced white layer (T-WL). These WLs exhibited distinct gradient microstructures from machined surface to bulk, suggesting different formation mechanisms.
- When machining at a V_c: 60 m/min, f: 0.05 mm/rev, M-WLs were generated using fresh and worn inserts with advantageous higher compressive stresses at the machined surface. The thickness of the white layer increased significantly with the progression of the tool flank wear, accompanied by a larger material drag zone underneath it, which facilitated a smoother transition from the white layer to the unaffected material. The hardness of the M-WL and the underlying material drag region were found to be ~26 % and ~7 % higher, respectively, compared to the unaffected bulk material. The surface roughness (R_a) increased from 0.1 μm to 0.19 μm when comparing surfaces machined with fresh cutting tools to those machined using worn tool.

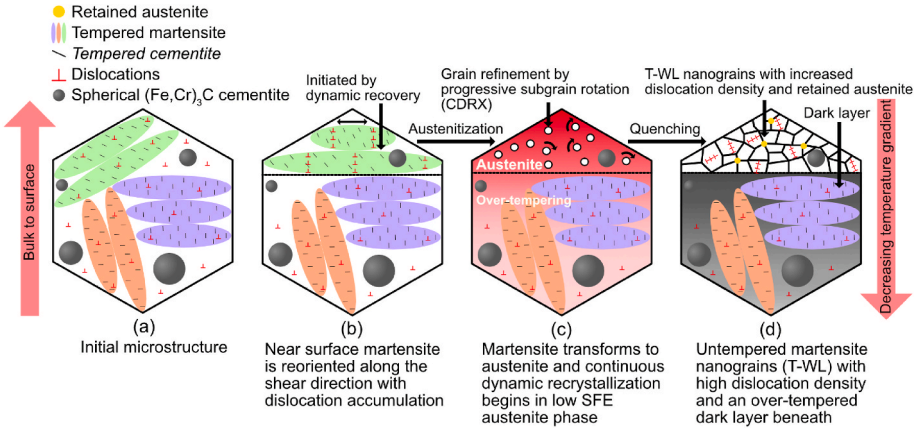

Fig. 12. Schematic illustration of T-WL microstructural development driven by the dynamic recovery mechanism, followed by dynamic recrystallization mechanism in association with reverse martensite transformation during hard turning.

- The microstructure development of the M-WL resulted in elongated and fragmented nanocrystalline grains down to ~10 nm, while the underneath material drag zone showed elongated plastically deformed grains with GNBs and IDBs. The M-WL formation is attributed to the dynamic recovery process, accompanied by severe plastic deformation and the grain subdivision mechanism.
- Machining at V_c: 110 m/min, f: 0.2 mm/rev resulted in the formation of T-WLs for both fresh and worn inserts. The formation of a T-WL was accompanied by a dark layer underneath. Tensile stresses were observed along the cutting direction due to higher thermal influence and the magnitude of tensile stress, thickness of the T-WL and the dark layer increased with tool flank wear. The T-WL exhibited ~27 % higher hardness, while the dark layer underneath showed a ~16 % lower hardness than the unaffected material. Moreover, the observed surface roughness is higher compared to M-WL with 0.59 μm for the fresh insert and 1.19 μm for the worn insert due to their high feed rate effect.
- The T-WL microstructure exhibited deformed and equiaxed nanocrystalline grains with increased dislocation density. The dark layer observed underneath consists of over-tempered martensite with no plastic deformation. The T-WL formation is due to initiated by dynamic recovery followed by dynamic recrystallization in association with reverse martensite transformation.

The findings show that the M-WL exhibited enhanced properties like higher compressive stresses, surface roughness (R_a) similar to grinding process and an improved nano hardness gradient on the machined surface, resulting in a superior tailored microstructure with cost-efficient hard turning process.

Data availability

Data will be made available on request.

Declaration of competing interest

The authors declare that they have no known competing financial interests or personal relationships that could have appeared to influence the work reported in this paper.

Acknowledgements

This work is part of the Turn2Flex project (Vinnova 2021-01274), under the Production 2030 strategic innovation program, supported by VINNOVA, the Swedish Energy Agency, and Formas. Special thanks to Sumitomo Electric Hartmetall GmbH, AB SKF, and Ovako AB for their support with materials and hard turning experiments. We would like to thank Mr. Adrian Harris and Mr. Gerard Irwin from Micro Materials Ltd. for their support with nanoindentation. This work was performed in part at the Chalmers Material Analysis Laboratory, CMAL.

References

[1] Liao Z, la Monaca A, Murray J, Speidel A, Ushmaev D, Clare A, Axinte D, M'Saoubi R. Surface integrity in metal machining - Part I: fundamentals of surface characteristics and formation mechanisms. Int J Mach Tool Manufact 2021;162:103687. https://doi.org/10.1016/j.ijmachtools.2020.103687.

[2] Mallick R, Kumar R, Panda A, Sahoo AK. Current status of hard turning in manufacturing: aspects of cooling strategy and sustainability. Lubricants 2023;11. https://doi.org/10.3390/lubricants11030108.

[3] Fang-yuan Z, Chun-zheng D, Xin-xin X, Min-jie W. Influence of cutting condition on white layer induced by high speed machining of hardened steel. Int J Adv Manuf Technol 2018;98:77–84. https://doi.org/10.1007/s00170-017-0454-3.

[4] Attanasio A, Umbrello D, Cappellini C, Rotella G, M'Saoubi R. Tool wear effects on white and dark layer formation in hard turning of AISI 52100 steel. Wear 2012;286–287:98–107. https://doi.org/10.1016/j.wear.2011.07.001.

[5] Liu M, Takagi JI, Tsukuda A. Effect of tool nose radius and tool wear on residual stress distribution in hard turning of bearing steel. J Mater Process Technol 2004;150:234–41. https://doi.org/10.1016/j.jmatprotec.2004.02.038.

[6] Chou YK, Evans CJ. White layers and thermal modeling of hard turned surfaces. In: ASME international mechanical engineering congress and exposition, proceedings (IMECE), 1997-W; 1997. p. 75–82. https://doi.org/10.1115/IMECE1997-1138.

[7] Hosseini SB, Klement U, Kaminski J. Microstructure characterization of white layer formed by hard turning and wire electric discharge machining in high carbon steel (AISI 52100). Adv Mater Res 2012;409:684–9. https://doi.org/10.4028/www.scientific.net/AMR.409.684.

[8] Kruth IP, Stevens I, Froyen I, Lauwers I. Study of the white layer of a surface machined by die-sinking electro-discharge machining. CIRP Ann-Manuf Technol 1995;44:169–72. https://doi.org/10.1016/S0007-8506(07)62299-9.

[9] Griffiths BJ. White layer formations at machined surfaces and their relationship to white layer formatins at worn surfaces, 107; 1984. p. 165–71.

[10] Hosseini SB, Klement U. A descriptive phenomenological model for white layer formation in hard turning of AISI 52100 bearing steel. CIRP J Manuf Sci Technol 2021;32:299–310. https://doi.org/10.1016/j.cirpj.2021.01.014.

[11] Li W, Sakai T, Li Q, Lu LT, Wang P. Reliability evaluation on very high cycle fatigue property of GCr15 bearing steel. Int J Fatig 2010;32:1096–107. https://doi.org/10.1016/j.ijfatigue.2009.12.008.

[12] Ramesh A, Melkote SN, Allard LF, Riester L, Watkins TR. Analysis of white layers formed in hard turning of AISI 52100 steel. Mater Sci Eng, A 2005;390:88–97.

[13] Barry J, Byrne G. TEM study on the surface white layer in two turned hardened steels. Mater Sci Eng, A 2002;325:356–64.

[14] Hosseini SB, Klement U, Yao Y, Ryttberg K. Formation mechanisms of white layers induced by hard turning of AISI 52100 steel. Acta Mater 2015;89:258–67. https://doi.org/10.1016/j.actamat.2015.01.075.

[15] Guo YB, Sahni J. A comparative study of hard turned and cylindrically ground white layers. Int J Mach Tool Manufact 2004;44:135–45. https://doi.org/10.1016/j.ijmachtools.2003.10.009.

[16] Akcan S, Shah WIS, Moylan SP, Chhabra PN, Chandrasekar S, Yang HTY. Formation of white layers in steels by machining and their characteristics. Metall Mater Trans A Phys Metall Mater Sci 2002;33:1245–54.

[17] Hossain R, Pahlevani F, Witteveen E, Banerjee A, Joe B, Prusty BG, Dippenaar R, Sahajwalla V. Hybrid structure of white layer in high carbon steel - formation mechanism and its properties. Sci Rep 2017;7:1–12. https://doi.org/10.1038/s41598-017-13749-7.

[18] Kokkirala S, Holmberg J, Klement U, Lundstrom R, Iwasaki H, Hosseini SB. Effect of cutting parameters on the generated surface integrity of hard-turned martensitic AISI 52100 bearing steel. Proced CIRP 2022;115:154–9. https://doi.org/10.1016/j.procir.2022.10.066.

[19] Wu T, Chang L, Liang W, Li X, Guo L, Zhou X. Understanding the grain refinement and residual stress formation mechanisms of a Ni-based alloy during machining processes. J Mater Process Technol 2024;334:118641. https://doi.org/10.1016/j.jmatprotec.2024.118641.

[20] Zhang F, Duan C, Sun W, Ju K. Effects of cutting conditions on the microstructure and residual stress of white and dark layers in cutting hardened steel. J Mater Process Technol 2019;266:599–611. https://doi.org/10.1016/j.jmatprotec.2018.11.038.

[21] Yang YY, Fang HS, Huang WG. A study on wear resistance of the white layer. Tribol Int 1996;29:425–8. https://doi.org/10.1016/0301-679X(95)00099-P.

[22] Hosseini SB, Ryttberg K, Kaminski J, Klement U. Characterization of the surface integrity induced by hard turning of bainitic and martensitic AISI 52100 steel. Proced CIRP 2012;1:494–9.

[23] Noyan I, Cohen J. Residual stress: measurement by diffraction and interpretation. Springer; 2013.

[24] Oliver WC, Pharr GM. An improved technique for determining hardness and elastic madulus using load and displacement. J Mater Res 1992;7:1564–83.

[25] Klocke F, Brinksmeier E, Weinert K. Capability profile of hard cutting and grinding processes. CIRP Ann-Manuf Technol 2005;54:22–45. https://doi.org/10.1016/s0007-8506(07)60018-3.

[26] Jouini N, Revel P, Thoquenne G. Influence of surface integrity on fatigue life of bearing rings finished by precision hard turning and grinding. J Manuf Process 2020;57:444–51. https://doi.org/10.1016/j.jmapro.2020.07.006.

[27] Hughes DA, Hansen N, Bammann DJ. Geometrically necessary boundaries, incidental dislocation boundaries and geometrically necessary dislocations. Scr Mater 2003;48:147–53. https://doi.org/10.1016/S1359-6462(02)00358-5.

[28] Elbestawi MA, Srivastava AK, El-Wardany TI. A model for chip formation during machining of hardened steel. CIRP Ann-Manuf Technol 1996;45:71–6. https://doi.org/10.1016/S0007-8506(07)63019-4.

[29] Hosseini SB, Beno T, Klement U, Kaminski J, Ryttberg K. Cutting temperatures during hard turning—measurements and effects on white layer formation in AISI 52100. J Mater Process Technol 2014;214:1293–300. https://linkinghub.elsevier.com/retrieve/pii/S0924013614000399.

[30] Yousefi S, Zohoor M. Effect of cutting parameters on the dimensional accuracy and surface finish in the hard turning of MDN250 steel with cubic boron nitride tool, for developing a knowledged base expert system. Int J Mech Mater Eng 2019;14:1–13. https://doi.org/10.1186/s40712-018-0097-7.

[31] Sun M, Hao L, Li S, Li D, Li Y. Modeling flow stress constitutive behavior of SA508-3 steel for nuclear reactor pressure vessels. J Nucl Mater 2011;418:269–80. https://doi.org/10.1016/j.jnucmat.2011.07.011.

[32] Tsuji N, Gholizadeh R, Ueji R, Kamikawa N, Zhao L, Tian Y, Bai Y, Shibata A. Formation mechanism of ultrafine grained microstructures: various possibilities for fabricating bulk nanostructured metals and alloys. Mater Trans 2019;60:1518–32.

[33] Zhang B, Shen W, Liu Y, Tang X, Wang Y. Microstructures of surface white layer and internal white adiabatic shear band. Wear 1997;211:164–8. https://doi.org/10.1016/S0043-1648(97)00099-9.

[34] Duan CZ, Zhang LC. Adiabatic shear banding in AISI 1045 steel during high speed machining: mechanisms of microstructural evolution. Mater Sci Eng, A 2012;532:111–9. https://doi.org/10.1016/j.msea.2011.10.071.
[35] Zhang K, Wang ZB. Strain-induced formation of a gradient nanostructured surface layer on an ultrahigh strength bearing steel. J Mater Sci Technol 2018;34:1676–84. https://doi.org/10.1016/j.jmst.2017.12.012.
[36] Krauss G. Tempering of martensite in carbon steels. Woodhead Publishing Limited; 2012. https://doi.org/10.1533/9780857096111.1.126.
[37] Hosseini SB, Thuvander M, Klement U, Sundell G, Ryttberg K. Atomic-scale investigation of carbon atom migration in surface induced white layers in high-carbon medium chromium (AISI 52100) bearing steel. Acta Mater 2017;130:155–63. https://doi.org/10.1016/j.actamat.2017.03.030.
[38] Kagawa A, Okamoto T, Saito K, Ohta M. Hot hardness of (Fe , Cr) 3C and (Fe , Cr) TC 3 carbides. October 1984;19:2546–54.
[39] Outeiro JC, Dias AM, Lebrun JL. Experimental assessment of temperature distribution in three-dimensional cutting process. Mach Sci Technol 2004;8:357–76. https://doi.org/10.1081/MST-200038984.
[40] Hua J, Shivpuri R, Cheng X, Bedekar V, Matsumoto Y, Hashimoto F, Watkins TR. Effect of feed rate, workpiece hardness and cutting edge on subsurface residual stress in the hard turning of bearing steel using chamfer + hone cutting edge geometry. Mater Sci Eng, A 2005;394:238–48. https://doi.org/10.1016/j.msea.2004.11.011.
[41] Han S, Melkote SN, Haluska MS, Watkins TR. White layer formation due to phase transformation in orthogonal machining of AISI 1045 annealed steel. Mater Sci Eng, A 2008;488:195–204. https://doi.org/10.1016/j.msea.2007.11.081.
[42] Jang DY, Watkins TR, Kozaczek KJ, Hubbard CR, Cavin OB. Surface residual stresses in machined austenitic stainless steel. Wear 1996;194:168–73. https://doi.org/10.1016/0043-1648(95)06838-4.
[43] Sakai T, Belyakov A, Kaibyshev R, Miura H, Jonas JJ. Dynamic and post-dynamic recrystallization under hot, cold and severe plastic deformation conditions. Prog Mater Sci 2014;60:130–207. https://doi.org/10.1016/j.pmatsci.2013.09.002.
[44] Hines JA, Vecchio KS. Recrystallization kinetics within adiabatic shear bands. Acta Mater 1997;45:635–49. https://doi.org/10.1016/S1359-6454(96)00193-0.
[45] Meyers MA, Xu YB, Xue Q, Pérez-Prado MT, McNelley TR. Microstructural evolution in adiabatic shear localization in stainless steel. Acta Mater 2003;51:1307–25. https://doi.org/10.1016/S1359-6454(02)00526-8.
[46] Gholizadeh R, Shibata A, Tsuji N. Grain refinement mechanisms in BCC ferritic steel and FCC austenitic steel highly deformed under different temperatures and strain rates. Mater Sci Eng, A 2020;790:139708. https://doi.org/10.1016/j.msea.2020.139708.